Construction and Building Materials 517 (2026) 145697

Contents lists available at ScienceDirect

Construction and Building Materials

journal homepage: www.elsevier.com/locate/conbuildmat

High mechanical resistance - porous ceramics by cold sintering of volcanic ash from Mount Etna

Mattia Biesuz [a,b,c,*], Paulina Pazerauskaite [a,d], Levent Karacasulu [a], Milad Kermani [a], Marco Viccaro [e,f], Vincenzo M. Sglavo [a,b], Danilo Di Genova [c,**]

[a] Department of Industrial Engineering, University of Trento, Via Sommarive 9, Trento 38123, Italy
[b] INSTM, Via G. Giusti 9, Firenze 50121, Italy
[c] Institute of Science, Technology and Sustainability for Ceramics (ISSMC) of the National Research Council (CNR), Via Granarolo 64, Faenza, RA I–48018, Italy
[d] Institute of Chemistry, Vilnius University, Naugarduko 24, Vilnius LT-03225, Lithuania
[e] Università degli Studi di Catania, Dipartimento di Scienze Biologiche Geologiche e Ambientali, Corso Italia 57, Catania 95129, Italy
[f] Istituto Nazionale di Geofisica e Vulcanologia - Sezione di Catania, Osservatorio Etneo, Piazza Roma 2, Catania 95125, Italy

ARTICLE INFO

Keywords:
Cold sintering process
Volcanic ash
Mount Etna
Porous ceramics
Recycling

ABSTRACT

The disposal of the volcanic ashes from explosive eruptions, like those of Mount Etna (Sicily, Italy), poses significant health, environmental, and economic concerns. Herein, we show that the volcanic ashes can be transformed into porous ceramics by the cold sintering process (CSP) at temperatures lower than 200°C. The consolidation is aided by a liquid medium that can be either water or a caustic KOH solution and by the application of a few hundred megapascals. The obtained porous materials possess a residual porosity between 22% and 39%, depending on the sintering conditions (pressure, temperature, KOH concentration). The CSP ash exhibits a fairly low thermal conductivity between 0.6 and 1.1 W/m K, which matches the benchmark of common ceramic bricks fired at high temperatures, but with substantially improved mechanical resistance ranging from 13 to 70 MPa (well above traditional bricks). In summary, CSP offers a new avenue to recycle inorganic waste materials and transform them into industrial products with potential application in the building industry.

1. Introduction

The building sector is a major consumer of raw materials, accounting for approximately 40–50 % of global utilization [1,2] (~20 Gton in 2017 [3]) and around 40 % [1,4] of total energy consumption. Key materials include limestone, clays, quartz, and feldspar. Additionally, its CO_2 emissions are considerable, extending beyond those generated by hydrocarbon combustion in materials processing. A significant contributor is the calcination of carbonates like limestone, magnesite, and dolomite, used in ceramics, bricks, cement, and mortars. This process releases carbon dioxide through the carbonate decomposition, amounting to 44–52 % of the carbonate weight itself. The development of sustainable building materials is therefore a cornerstone for any public policy for green development, the urgency of which has recently been crucial for reducing environmental impact and aligns with global sustainability efforts, as emphasized in the United Nations' 17 *Sustainable Development Goals* within the 2030 Agenda.

The ceramic industry's decarbonization is still far from being achieved. While technological advancements in the efficiency of furnaces have certainly been accomplished throughout the decades, it only accounts for marginal improvements in terms of energy consumption. A possible answer, though still confined to the lab scale, is based on the introduction of innovative processing routes and, specifically, non-conventional sintering processes [5]. While some of these approaches, like flash sintering, spark plasma sintering, and microwave sintering, cause a substantial reduction of the firing time and temperature, others, like the cold sintering process (CSP), promise an even larger impact by reducing the consolidation temperature to near ambient values [6–9].

CSP was first introduced by Randall and co-workers at Penn State University in 2016 [10] following earlier works on the hydrothermal consolidation of ceramics [7]. CSP is based on a pressure-assisted transient liquid phase consolidation, although the mechanistic

* Corresponding author at: Department of Industrial Engineering, University of Trento, Via Sommarive 9, Trento 38123, Italy.
** Corresponding author.
E-mail addresses: mattia.biesuz@unitn.it (M. Biesuz), danilo.digenova@cnr.it (D. Di Genova).

https://doi.org/10.1016/j.conbuildmat.2026.145697
Received 1 November 2025; Received in revised form 13 February 2026; Accepted 18 February 2026
Available online 24 February 2026

understanding is still controversial [11,12]. The ceramic powder is mixed with a solvent, usually a water solution, and pressed below 350°C under a few hundred megapascals. Since its invention, CSP has been applied to different classes of functional ceramics (bioceramics, piezoelectric, ferroelectric… [13–21]); conversely, the literature on its application to the building sector is still modest. Currently, one can find just a few works on CSP applied to calcium carbonate [22–25], construction demolition wastes [26,27], geopolymers [28–30], and sand-gypsum composites [31]. While the functional ceramic industry could undoubtedly benefit from CSP in terms of microstructural tailoring and enhanced properties, addressing sustainability challenges requires its application in energy-intensive sectors, with the building industry certainly being the most significant among them.

Among the various raw materials that can contribute to a sustainable production cycle for the building industry, volcanic ash represents a promising yet underutilized resource. Volcanic ash is a type of pyroclast, referring to fragmented rock material ejected during a volcanic eruption due to the explosive fragmentation of magma [32]. It consists of fine particles, typically lower than 2 mm [33] and is composed of a mixture of silicate glasses and crystalline mineral phases, including feldspars, pyroxenes, olivine, and transition metal oxides such as iron and titanium oxides [34,35].

Due to its fine-grained size, volcanic ash can be transported by wind over vast distances before settling, creating serious environmental, infrastructural, and health-related challenges [36–42]. The large volumes of ash generated during eruptions pose significant waste management issues for governments and communities. One of the most notable examples is Mount Etna volcano in Italy, which has produced about 290 violent explosive events (known as paroxysmal eruptions) throughout the period 1986–2024 [43–45], generating eruptive columns in the range 5–15 km above the sea level that caused conspicuous ash dispersion into the troposphere and severe fallout of the pyroclastic material on the volcano flanks. Each paroxysmal eruption is able to release volumes in the order of 10^5-10^6 m^3, with cumulative quantities that, in specific periods of activity, like the most recent 2020–22 sequence, exceed 10^7 m^3 [46].

Based on these considerations, volcanic ash has generated significant attention in the scientific community as a potential resource for sustainable reuse and valorization [47–61]. A smaller portion of the literature has explored its use as a binder component in cementitious products or as a temper in brick and tile manufacturing [61], whereas the majority of the existing studies have focused on the incorporation of volcanic ash into alkali-activated/geopolymer materials. Alkali-activated materials (geopolymers) are inorganic structures produced through the dissolution and re-polymerization of aluminosilicate precursors under alkaline conditions on a timescale [55,56,58], yielding cement-like networks that have recently demonstrated real-world applicability, including use in heritage restoration works such as cathedral masonry repair [62].

All these applications are valuable; however, they still rely on relatively long treatment times and/or high-temperature processing, and typically employ volcanic ash only as a partial constituent of the overall feedstocks. The CSP enables low-temperature densification of inorganic powders through interfacial dissolution and precipitation mechanisms, offering relatively short processing times along with significant energy-efficiency and sustainability advantages [6–9,63,64]. In addition, scalability and component size are under active development, with recent demonstrations indicating feasibility beyond laboratory-scale pellets [65,66]. Therefore, the CSP represents a promising alternative, enabling the direct consolidation of volcanic ash at significantly lower temperatures while maximizing its utilization as the primary raw material.

In this study, we explore how the cold sintering process (CSP) can be employed to produce porous ceramics by recycling volcanic ash from Mount Etna. This approach offers multiple advantages: it reduces CO_2 emissions associated with ceramic manufacturing, promotes waste valorization, and decreases the demand for virgin raw materials, thereby mitigating the environmental impact of traditional mining activities and, overall, of the production of building materials.

2. Methods

The ashes of this study were collected on the upper southern flank of Mount Etna and are associated with pyroclastic deposits from the 2020–22 paroxysmal activity. The main chemical composition of the ash by weight was SiO_2 (46.9 %), Al_2O_3 (16.2 %), FeO_{tot} (11.5 %), CaO (10.8 %), MgO (5.59 %), Na_2O (3.32 %), K_2O (1.89 %), TiO_2 (1.91 %), MnO (0.21 %), P_2O_5 (0.46 %), and the LOI (1.28 %). A detailed textural and compositional description of the ashes can be found in [43]. The ashes were first ground in an agate mortar to comminute them below 1 mm. The obtained powder was then ball-milled in deionized water (DIW) using a Turbula mixer for 24 h to further reduce particle size. 5 mm diameter alumina spheres filled half of the milling jar, where a slurry containing 1:1 wt ratio of powder and DIW was added.

The particle size distribution of the obtained powder was analyzed by a laser scattering particle size analyzer (Partica LA-960 V2, Horiba, Japan) in aqueous medium, assuming a refractive index of 1.58 [67]. The results show a reduction of the particle size down to about 0.8 μm (d_{50}) with monomodal distribution after 24 h of ball milling (Fig. 1).

A sketch summarizing the workflow from the volcanic ash to the final cold-sintered product is shown in Fig. 1. The CSP samples were prepared by mixing 0.6 g of milled ash with KOH (CAS#:1310–58–3, J.T.Baker, Holland) water solutions of various molarity (from 0 to 5 M). The amount of liquid for most of the experiments was 20 wt% with respect to the powder; some experiments were carried out using a liquid amount of 25 wt%. The powder and the liquid were mixed in an agate mortar until a homogeneous paste was achieved. Then, the mixture was introduced into a cylindrical tool steel die (Φ=13 mm). A uniaxial pressure (ranging from 100 MPa to 500 MPa) was applied using a universal testing machine (MTS 810, Material Testing System, USA). A heating jacket around the die was used to heat the sample to various temperatures (from room temperature to 250 °C) with a heating rate of 10 °C/min. The temperature was monitored with a K thermocouple and lab-view software. The heating cycle started just after the uniaxial pressure application, which was kept constant throughout the whole process. Most of the samples were isothermally held at the CSP temperature for 15 min; some experiments with longer (60 min) and shorter (5 min) holding times were also performed. After CSP, the system was free-cooled. To ensure a consistent comparison, all specimens were dried at 130 °C, regardless of their cold sintering temperature (from room temperature to 250 °C). Although this additional heating step may promote limited geopolymerization in the room-temperature specimens, such changes are expected to be minor and not influential on the macroscopic physical properties (like density/porosity).

The bulk density was determined by Archimedes' method using the ASTM C830 standard as a reference. Distilled water was used as the buoyancy medium, and the weights were measured with an analytical balance with a sensitivity of 0.1 mg. The milled ash real density, equal to 2.81 g/cm^3, was assessed by a He-pycnometer (Ultrapyc5000 from Anton Paar®). Microstructural analysis was carried out on fresh fracture surfaces by scanning electron microscopy (SEM, SUPRA V40, Carl-Zeiss, Germany). Before the analysis, the samples were coated with a thin Pt/Pd film by sputtering.

The mineralogical composition was evaluated by X-ray diffraction (XRD) using an Italstructures IPD3000 diffractometer equipped with a copper anode (λ = 1.5406 Å, 40 kV, 30 mA). Fourier transform infrared spectroscopy spectra (FTIR) were acquired in ATR mode (attenuated total reflectance) between 650 and 4000 cm^{-1}. Four scans were recorded for each sample with a resolution of 4 cm^{-1} using a Perkin-Elmer FT-IR Spectrometer (Perkin-Elmer, USA).

The thermal properties (conductivity, diffusivity, specific heat) of selected samples were assessed. Thermal diffusivity was measured using Netzsch 467 HyperFlash (Selb, Germany) using the laser flash method.

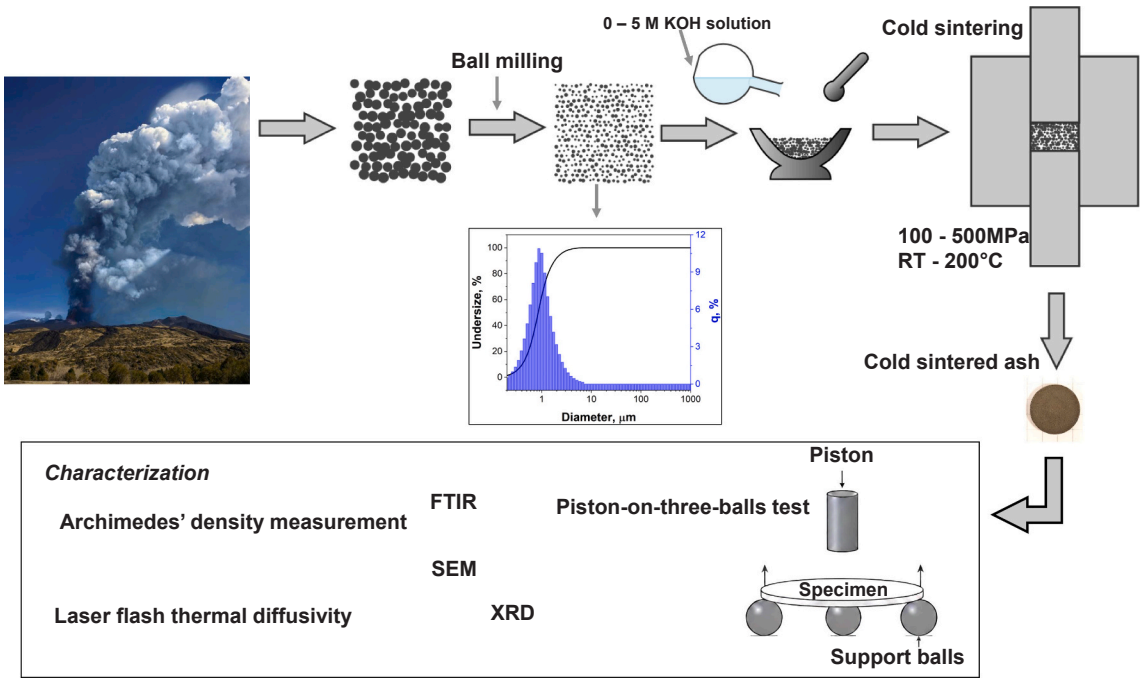

Fig. 1. Schematic of the cold sintering process used for the volcanic ash consolidation, the Mount Etna picture was taken during the March 2020 eruption. The center inset shows the particle size distribution (PSD) of the milled ash. Schematic of the flexural strength test in a piston-on-three-balls configuration and other characterization techniques are reported in the bottom panel.

The pulse width was 0.5 ms, the discharge voltage 250 V, and the spot size 3.7 mm. Data were collected every 20 °C in the temperature range 20–100 °C. Before the measurement, the samples were coated with a layer of graphite. The data were fitted through the transparent model from the device library. To calculate the thermal conductivity values, the specific heat was measured by DSC (METTLER TOLEDO DSC 5 +) carried out at 10 °C/min in the temperature range −20–110 °C in a controlled atmosphere (nitrogen flow 100 mL/min). The equibiaxial flexure test (piston-on-three-balls) was used to determine the mechanical strength of the cold sintered material. A comprehensive description of the flexural three-ball testing procedure has been reported elsewhere [68]. The tests were performed on 4 samples for each condition using a universal testing machine (MTS 810, Material Testing System, USA) equipped with a 100 kN load cell. The specimen (Φ=13 mm) was placed on three supporting balls, equally spaced at120°, and loaded by a steel piston (Φ=2 mm) moving at 2 mm/min. The biaxial flexural strength was determined as follows (Eq.1):

$$\sigma = \frac{3P((1+\nu)}{4\pi t^2}\left[1+2\ln\frac{a}{b}+\frac{(1-\nu)}{(1+\nu)}\left\{1-\frac{b}{2a^2}\right\}\frac{a^2}{R^2}\right] \quad (1)$$

P being the failure load, t the sample thickness, ν Poisson's ratio, b the radius of the piston, R the radius of the sample, and a the radius of the circle of the support.

To better elucidate the mechanism, dissolution tests were performed on the blend prepared from the milled ash and KOH solution (1:1 by weight), ensuring complete wetting of the powder, following a similar approach reported in a previous study [69]. The mixture was ultrasonicated in a polypropylene falcon tube for 1 min and subsequently left to stand at room temperature for 1 h, approximating the total interaction time used in CSP experiments. The dissolved species were then extracted into deionized (DI) water to a total volume of 50 mL. The resulting suspensions were ultrasonicated for 10 min and centrifuged at 6000 rpm for 15 min to collect the supernatant. The cation concentrations in the supernatant were quantified using inductively coupled plasma–optical emission spectroscopy (ICP-OES, Perkin Elmer Avio 550 Max, Shelton, USA) and corrected using a prepared KOH-containing blank.

Thermal analysis of the sample achieving the highest density in CSP was performed using a simultaneous thermal analyzer (STA 449 F3 Jupiter, Germany) coupled with FTIR gas analysis, with the gas cell maintained at 200°C. To ensure reliable detection of the Gram–Schmidt signal, approximately 90 mg of sample was placed in an alumina crucible and heated to 850 °C at a rate of 40 °C min^{-1}. The measurements were performed under a continuous flow of synthetic air at 50 cm^3 min^{-1}, and infrared spectra were continuously recorded to identify gaseous decomposition products.

3. Results

The key parameters governing the consolidation during CSP are the molarity of the KOH solution, the process temperature, and the applied pressure (Fig. 2a,a'). Some preliminary activity showed that the CSP time has a modest effect on the consolidation, and changing it from 5 min to 60 min. For instance, at 200 °C a relative density of ~73.4 % was obtained using 2 M KOH solution after 60 min, while a comparable value of ~73.0 % was reached with a reduced dwell time of 15 min. The difference between these two conditions is less than 1 %, indicating that extending the dwell time to 60 min does not significantly enhance densification. When the dwell time was further reduced to 5 min, the relative density decreased to ~71.5 %, demonstrating a more substantial deviation. Considering both the energetic benefit and the necessity to allow sufficient dissolution–reprecipitation kinetics, the experiments were therefore carried out using a fixed time of 15 min for the present study. Similarly, an increase in the solution amount from 20 to 25 wt% had a marginal impact on the final density.

The relative density generally increases with the KOH molarity in the solution (i.e., with the pH) or when higher temperature and pressure are used, and, consequently, the porosity (100 − relative density) decreases. The porosity values, reported for the different sintering conditions in Tab.S1 (Supplementary Material), confirm the porous nature of the sintered artifacts (≈ from 22 % to 39 %). Most of the improvements in terms of temperature occur between 50 and 200°C, the density plot exhibiting a sigmoidal shape characteristic of a typical sintering curve. When the temperature is above 200°C, a saturation is reached and the

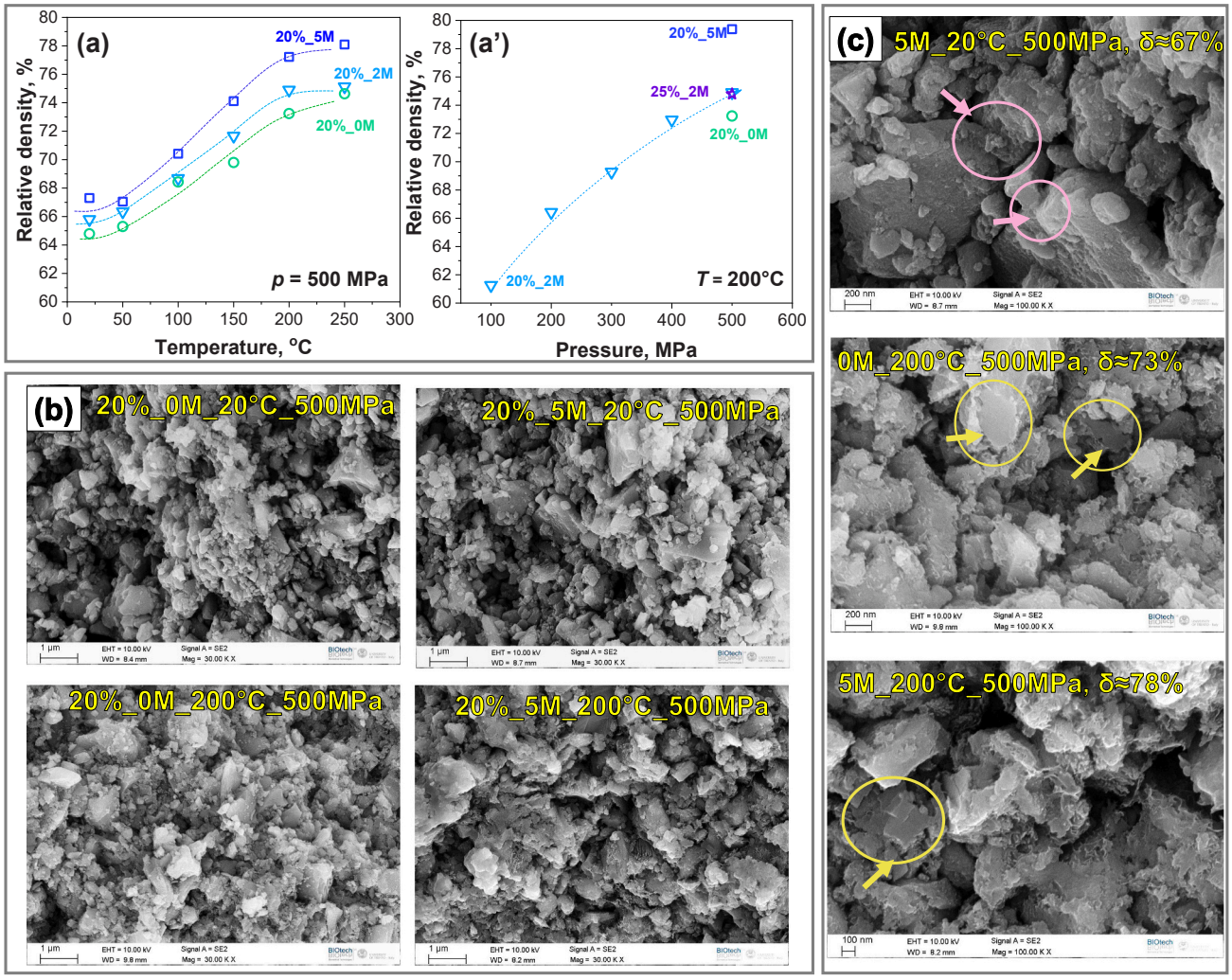

Fig. 2. Physical and microstructural evolution of the volcanic ash during CSP with a duration of 15 min. Relative (bulk) density evolution as a function of (a) CSP temperature (pressure = 500 MPa) and (a') pressure ($T = 200°C$). The KOH solution molarity is also shown. The dashed lines are just guides for the eye. SEM micrographs of the fracture surface of Etna's ashes cold sintered under various conditions at (b) low and (c) high magnification. The yellow and pink arrows in (c) indicate regions characterized by intra-particle cleavages and by the formation of necks in the early sintering stages, respectively.

density plot flattens. On the other hand, no saturation is recorded when considering the pressure-density plot up to 500 MPa.

The SEM micrographs at low (Fig. 2b) and high (Fig. 2c) magnification highlight a substantial evolution of the microstructure from a low-density system characterized mainly by distinct particles still largely maintaining the geometry of the parent powder to a quite dense material with reduced porosity. Interestingly, already at room temperature, despite the modest densification, inter-particle necking occurs (shown by the pink arrows in Fig. 2c), thus providing robust evidence for the activation of some mass-transport phenomena already at room temperature. The powder morphology is, however, substantially different at 200°C (both for 0 and 5 M KOH solutions), the micrographs showing the formation of a "curly" surface indicating a stronger reaction with the liquid medium. Interestingly, the samples cold sintered at 200°C also show regions where the crack propagated across the particles, not simply following the inter-particle regions. Additional micrographs are available in Supplementary Materials.

The mineralogical composition of the ash does not evolve during CSP (Fig. 3a). All tested materials contain crystalline phases, including silicates, namely tectosilicates (Ca-plagioclase, i.e., anorthite), pyroxenes (augite), and nesosilicates (olivine), and a mixed Fe/Ti magnetite. In addition to the crystalline components peaks, the XRD diagrams show an amorphous hump.

The vibrational spectra (ATR-FTIR Fig. 3b) do not show substantial evolution with CSP, as well. The ATR spectra are dominated by the asymmetric stretching of M-O tetrahedra (M being predominantly Si) with peaks at 960–970 cm^{-1}. The ATR peaks below 1000 cm^{-1} correspond to a largely depolymerized glass network rich in non-bridging oxygen [70] while pure silica glass accounts for a peak around 1100 cm^{-1} [71]. No substantial signal originating from water or Si-OH vibrations can be detected in the spectra (note that after CSP at RT, the samples were still dried at 130°C overnight before the tests). In addition, the band observed around ~1450 cm^{-1} can be attributed to carbonate formation (asymmetric stretching of CO_3^{2-}), consistent with previous reports on cement/geopolymer systems where similar features have been oserved [57,72].

The TGA plot of the sample CSPed under 500 MPa at 200°C with the 5 M KOH solution (i.e., the densest one) is reported in Fig. 4 along with the Gram-Schmidt curve. The total weight loss is about 4 wt%with the weight stabilizing at 750°C. A first weight loss starts from about 100°C and steadily evolves up to 400°C and accounts for more than 3 wt% of evolution, a second smaller event is localized between 550°C and 750°C. The FTIR analysis of the evolved gases (Fig. 4b,c) shows a significant water evolution from 100°C to about 400°C, while CO_2 evolves at higher temperatures with two distinct peaks at 335 and 650°C.

As CSP was carried out in a "closed" die configuration, a direct

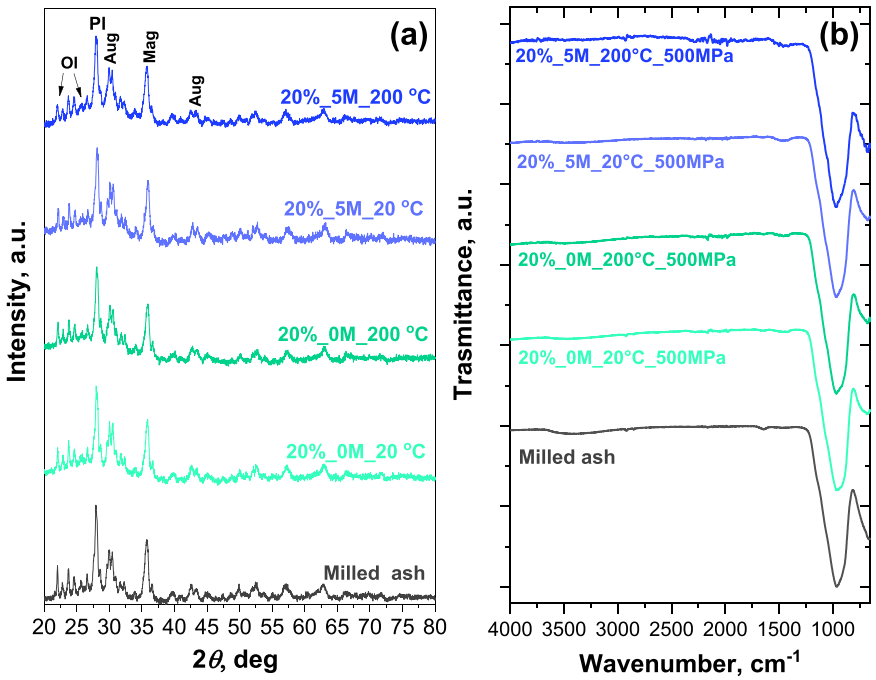

Fig. 3. (a) XRD patterns of the pristine ash and the cold sintered materials for different KOH solution molarity and processing temperature (pressure = 500 MPa). Pl = Ca-plagioclase (anortite), Aug = augite, Ol = olivine, Mag = Ti-magnetite (i.e., $Fe^{2+}(Fe^{3+},Ti^{3+})_2O_4$). (b) FTIR spectra (ATR mode) of the pristine ash and the cold sintered materials for different KOH solution molarity and processing temperature (pressure = 500 MPa). The samples consolidated were dried overnight at 130°C.

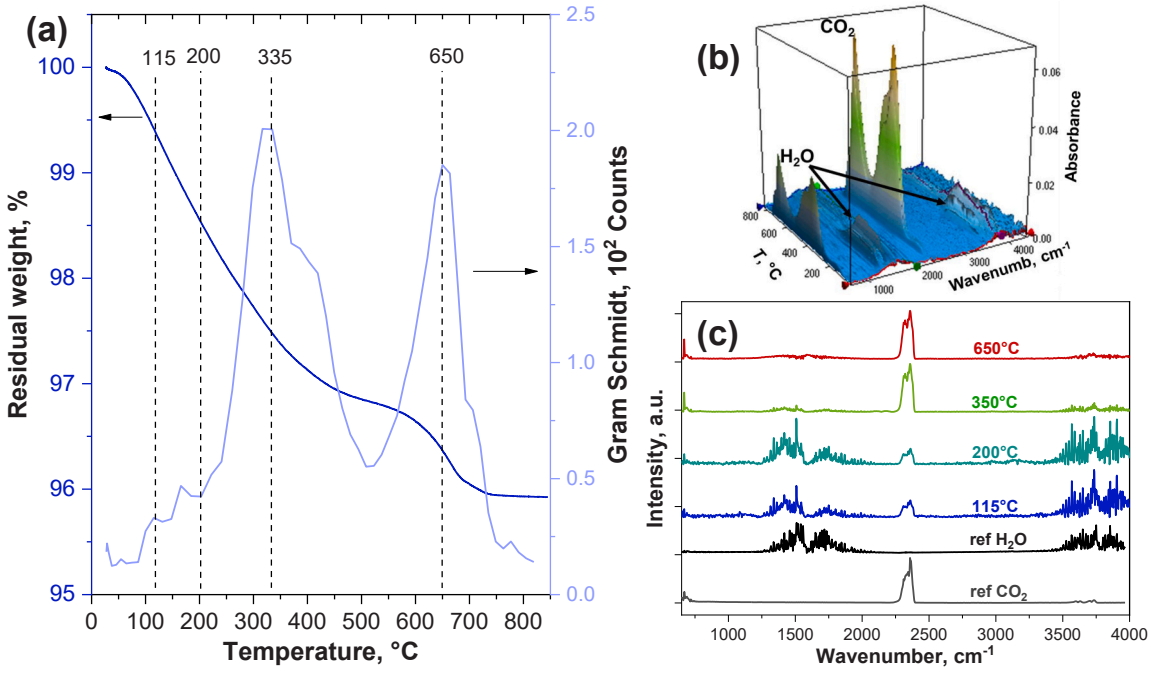

Fig. 4. (a) TGA and Gram-Schmidt curve as a function of temperature for 20 %_5M_200°C_500MPa sample; (b) FTIR absorbance evolution measured on the gas evolved from the sample in TGA, and (c) representative FTIR spectra at different temperatures. The reference spectra for carbon dioxide and water are also provided.

identification of the dissolution products is unfeasible [69]. Therefore, separate dissolution tests were performed to assess which elements preferentially dissolve and may assist densification. The ICP-OES results are summarized in Table 1. Changes in Al, Si, Fe, Mg, Ca, and Na concentration were observed in the solution corrected by the blank KOH sample. ICP measurements (mmol/L) revealed that Na dissolved most extensively, with Si, Al, Ca and Mg following in decreasing order.

The thermal diffusivity (TD) measured between room temperature and 100°C is shown in Fig. 5a where the trends mirror the evolution of density, with materials processed at higher temperatures, pressures, or with more concentrated KOH solutions exhibiting higher diffusivity. The evolution of TD as a function of density is shown in Fig. 5b. It clearly increases with density, although differences are observed between samples processed at 200°C and 20°C, CSP carried out at room temperature generally results in lower TD materials.

The thermal conductivity (TC) between 20 and 100°C, calculated

Table 1
Dissolution data for the milled ash prepared with 0, 2, and 5 M KOH solution. Concentrations of the dissolved species are reported in mmol/L, as determined by ICP-OES.

	0 M (mmol/L)	2 M (mmol/L)	5 M (mmol/L)
Al	0.1746	0.4292	0.6277
Si	0.3771	0.8293	0.9546
Fe	0.0500	0.0213	0.0063
Mg	0.0736	0.0252	0.0076
Ca	0.0924	0.0962	0.0704
Na	1.0505	2.5816	3.0755

from the TD data and the specific heat (not reported), is shown in Fig. 5c. There is a general increase of TC as a function of the measuring temperature. Similarly to TD data, TC also increases with density and, therefore, is higher when CSP is carried out at 200°C or when a concentrated KOH solution is employed (Fig. 5d). The room temperature TC ranges between 0.7 and 1.1 W/m K depending on the processing conditions (Table 2).

The mechanical strength of the CSP bodies was assessed by the piston-on-three-balls method (equibiaxial flexure, Table 2). While the strength for the samples consolidated at RT is in the order of 10–20 MPa, it substantially increases at 200°C, reaching values of about 60 – 70 MPa.

4. Discussion

Cold sintering process (CSP) offers a promising approach for the valorization of waste silicate materials such as volcanic ash. In this study, we focused on volcanic ash from Mount Etna (Sicily, Italy), a highly active volcano that experiences frequent eruptions each year. These eruptions generate plumes reaching up to 15 km above the sea level and release ash volumes of up to 10^7 m^3 annually [73].

Explosive eruptions are particularly relevant for two reasons. First, they disperse volcanic ash over a vast region, leading to significant environmental, infrastructural, and health concerns. The widespread deposition of ash results in high disposal costs, making its recycling into value-added products an attractive alternative. Second, explosive eruptions produce magma that does not form monolithic blocks (i.e., lava) in the form of aggregates of various sizes. Due to the rapid cooling of the ejected melt, the resulting ash is often highly porous and contains

Table 2
Room temperature (20°C) thermal conductivity and biaxial bending strength for volcanic ash CSP at 20°C and 200°C with water and 5 M KOH solution.

Samples	TC_{RT}, W/mK	Bending strength, MPa
20 %_5M_20°C_500MPa	0.76 ± 0.03	18.4 ± 4.8
20 %_5M_200°C_500MPa	1.13 ± 0.03	74.1 ± 12.9
20 %_0M_20°C_500MPa	0.60 ± 0.01	13.2 ± 0.3
20 %_0M_200°C_500MPa	0.83 ± 0.03	60.6 ± 8.8

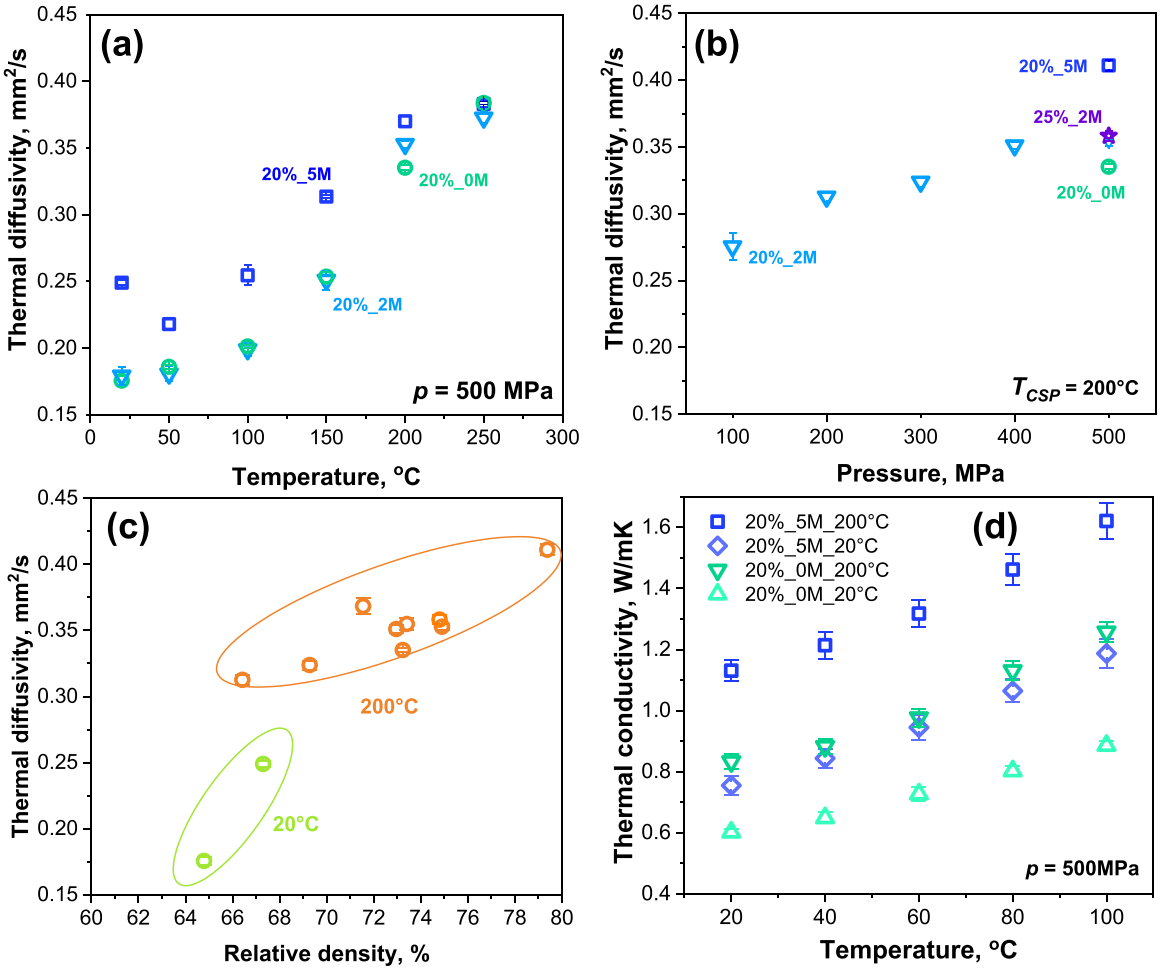

Fig. 5. Thermal diffusivity measured between RT and 100°C as a function of the CSP (a) temperature and (b) pressure. The effect of other parameters like KOH molarity is also shown. (c) Thermal diffusivity as a function of relative density for samples CSP at RT and 200°C. (d) Thermal conductivity between 20 and 100°C for volcanic ash CSP at 20°C and 200°C using water and a 5 M KOH solution (pressure = 500 MPa).

a substantial glassy phase, aspects which facilitate its excavation, processing, and cold sintering.

The porous nature of ash generated by explosive eruptions provides an advantage in milling processes, allowing comminution to submicron sizes within just 24 h of ball milling. Additionally, the presence of a reactive amorphous phase enhances the solubility of the material, which is a key parameter for the success of CSP-based consolidation. Although this study focused on Mount Etna ashes, the approach could be extended to other volcanic systems exhibiting similar explosive behavior. The findings suggest that volcanic ash from explosive eruptions has great potential as a sustainable raw material for advanced ceramic applications.

CSP enables the production of porous ceramics using volcanic ash as the sole raw material, supplemented only with a water solution. This represents a significant advantage compared to previous studies, where volcanic ash was used merely as a tempering agent in tile production [47,50]. In this regard, CSP allows the incorporation of the recycled component in a substantially larger amount compared to the literature, where its use is limited to only 10–20 % of the raw materials batch. Besides the possibility of using large amounts of ash, CSP offers obvious environmental advantages over the conventional firing processes in terms of energy consumption and carbon footprint (note that about 60–70 % of the energy consumed by the ceramic industry is used for firing).

The density and microstructural (Fig. 2) evolution during CSP are primarily influenced by the solution composition, processing temperature, and pressure. Conversely, factors such as solution quantity (15–25 wt%) and the sintering time (5 –60 min) have only a minor impact on final properties. As expected, higher temperature and pressure enhance densification by accelerating mass transport kinetics, promoting dissolution phenomena, and increasing the driving force for sintering. The effect of temperature seems to saturate above 200°C, with only small improvements at 250°C. This might be related to water evaporation during CSP at temperatures exceeding 200°C. On the other hand, the effect of pressure does not saturate (Fig. 2a') up to 500 MPa. Further, improvements in terms of density are possible by applying higher pressure but are constrained by technological limitations (spring back of the ceramic pellet, wear of the die punches, yielding of the pressing tooling etc.). The KOH molarity also plays a significant role, similar to other silicate systems [74–76]. In fact, the solubility of silica is greatly enhanced in a caustic environment, which in turn promotes higher density levels [77].

In some samples processed at room temperature, clear inter-particle necking by particle-particle contact points is visible (Fig. 2c), thus indicating the activation of mass transport phenomena at ambient temperature [78]. On the other hand, a substantial reaction of the powder with the solution can be spotted at 200°C with the formation of a rounded morphology of the particle's surface, all resulting in densification via dissolution-precipitation [79]. This reactivity is responsible for the substantial enhancement in the pellet density, which increases by about 10 % between RT and 200°C. Despite some reaction occurring between the solvent and the powder, still, no substantial macroscopic evolutions in terms of vibrational features and XRD patterns can be pointed out (Fig. 3). The CSP porous ceramics are therefore similar to the starting ash from a mineralogical and structural point of view, containing magnetite, plagioclase, augite, olivine, and a depolymerized glass. These results are consistent with the literature, highlighting compounds that are usually found in the ash produced during explosive eruptions [34]. It is also worth noting that cold sintering of inorganic powders predominantly promotes densification through limited dissolution–reprecipitation and the development of thin amorphous/glassy interparticle films, rather than through reconstructive phase transformations of the majority of the material's volume detectable by XRD. In such a case, the crystalline phases observed before and after CSP remain the same. This behavior has also been demonstrated in several silicate or ash-based systems subjected to CSP. For example, diatomaceous earth powders processed via cold sintering showed no phase transformation by XRD, and densification was attributed to the interaction between the CSP solution and the silicate glass present in the compound [76]. Likewise, regolith-like silicate powders exhibited unchanged phase compositions after CSP [69]. Furthermore, in metakaolin/geopolymer-like systems treated under CSP conditions, no crystalline phase transformation was detected; instead, the amorphous phase increased, suggesting a partial dissolution of the crystals and their precipitation in an amorphous state [80].

The thermal diffusivity increases with relative density and is therefore dependent on the CSP parameters (Fig. 5). Materials cold sintered at RT and 200°C can be grouped in two different regions in the density *vs.* TC space (Fig. 5c), with those processed at room temperature possessing lower TC than those processed at 200°C at a similar density level. This might be due to the presence of a small amount of residual water after CSP at RT (actually, these samples also possess a larger heat capacity determined by DSC - data not reported).

The thermal conductivity (Fig. 5d) increases with temperature, similarly to many other amorphous systems [81]. The typical RT values for TC are about 0.6–0.8 W/m K and 0.8–1.1 W/m K for samples processed at RT and 200°C, respectively. Such TC is similar to traditional brick materials fired at high temperatures, typically ranging between 0.5 and 1.4 W/m K [82–84]. However, the bending strength of the CSPed ash is fairly high: 10–20 MPa and 60–70 MPa after CSP at RT and 200°C, respectively (Table 2). These values are generally well above those of traditional ceramic bricks, which typically do not exceed 10 MPa [85–87].

The excellent mechanical properties of the samples cold sintered at 200°C are reflected in the SEM micrographs (Fig. 2). These highlight the cleavage of some particles, thus underscoring the high strength of the interparticle bonding during CSP. We can also observe from Table 2 that the samples consolidated with 5 M KOH solution at 20°C and with water at 200°C possess similar TC, but the mechanical strength of the latter is three times that of the former. In other words, CSP at 200°C enhances the mechanical properties more than the thermal conductivity compared to processing at 20°C. Again, this can be correlated to the stronger interparticle bonding formed in "warm conditions". Consequently, the increase in flexural strength and thermal conductivity is consistent with the SEM-observed neck thickening and reduction in intergranular pore volume with increasing temperature and molarity.

Highly alkaline media induce silica depolymerization silicate species [69,88,89]. These species may reorganize into more ordered networks during CSP. Although the dissolution data reflect only the room-temperature behavior of the ash in the absence of pressure, they support the notion that CSP promotes partial dissolution and stress-assisted densification through a dissolution–reprecipitation mechanism [69,90]. Confirming our work, a previous dissolution study on the volcanic ash in NaOH environments has already shown that the silicon load in solution is larger than the Al one [91].

Based on the dissolution test results, the Si/Al ratio decreased with increasing alkali molarity, from approximately 2.2 at 0 M to about 1.5 at 5 M. These values fall within the range generally considered favorable for geopolymerization, indicating suitable conditions for the formation of aluminosilicate networks [92]. In addition, the Ca/Si ratio showed a pronounced decrease with increasing molarity, decreasing from approximately 0.25 at 0 M to 0.12 at 2 M, and further to 0.07 at 5 M. The relatively higher Ca/Si ratio observed at 0 M may suggest a greater contribution of Ca-rich binding phases. Accordingly, the satisfying mechanical properties measured for the samples prepared at 200°C with 0 M can be attributed to the increased formation of C–S–H or C-alkali oxides-A-S-H type phases, which are known to enhance mechanical strength due to their dense and compact gel structure [93,94]. Such gel is expected to precipitate at the particle neck region, providing inter-particle bonding.

Besides the formation of geopolymer-like gel, carbonates form from the reaction of metal oxides with the atmospheric CO_2. Such a reaction is

facilitated by the "wet conditions" of CSP, similar to the reaction pathways occurring during the setting of burnt lime. The presence of carbonates is clearly evidenced by their vibrational features in FTIR (Fig. 3b). However, they are not visible in XRD, likely due to their nanocrystalline/defective nature or because they are present in small amounts, below the detection limit of the instrument. This makes a clear identification of the carbonate stoichiometry not trivial, though one can suppose they mostly involve alkaline and alkaline earth oxides. The carbonate formation is further confirmed by the FTIR-coupled TGA, pointing out of CO_2 evolution through two main thermal events occurring at 335 and 650°C.

The geomplymer-like gel can be partially, but not entirely, dehydroxilated during CSP (if carried out at 200°C) or during the drying step (130°C). The TGA analysis (Fig. 4) points out a small but detectable water evolution localized between 80 and 400°C. The weight loss at lower temperatures can be primarily attributed to adsorbed water from environmental humidity. Even if the sample was dried at 130°C the night before TGA, still some water was adsorbed during its handling in the atmosphere (these highly hygroscopic species could be the carbonates). However, a substantial water signal above 150°C, confirms the presence of structurally-bounded water.

The cold sintering process enables the densification of the volcanic ash at remarkably low temperatures by employing a transient liquid phase together with external pressure. Geopolymerization relies on selective bulk dissolution of reactive aluminosilicate phases followed by gel formation and polycondensation with longer treatment times (generally progressing over hours to days at ambient or mildly elevated temperatures) [56], whereas cold sintering involves interfacial dissolution and solution-mediated precipitation at grain boundaries in a relatively short time (typically within minutes to hours), yielding densification without forming a new continuous main binder phase. Despite these differences, both routes rely on aqueous-assisted dissolution–transport–reprecipitation (or polycondensation) mechanisms, albeit at different length scales and yielding different outcomes. This also suggests that, under comparable alkaline and aqueous conditions, a geopolymer-like dissolution and reprecipitation process may occur locally at particle boundaries during cold sintering.

Note that in pressure-less conditions (geopolymer-like processing), the consolidation of the ash is expected to be very modest using the said molarity/solution content. In fact, under 100 MPa the material density (about 60 %) is very close to that of a green body.

The overall results point out that CSP can be used to use volcanic ashes to produce porous ceramics with fairly low thermal conductivity and excellent mechanical strength compared to traditional ceramic bricks.

5. Conclusions

The cold sintering process (CSP) proves to be an effective and energy-efficient method for producing porous ceramics using volcanic ash as a raw material. The evolution of microstructure and density during CSP is primarily influenced by temperature, pressure, and solvent chemistry. Typical processing conditions involve temperatures below 200°C, pressures of a few hundred MPa, and a caustic medium (such as KOH solutions). Notably, significant consolidation of the ash can also be achieved using distilled water as a transient liquid phase. It is therefore plausible that cold sintering may trigger a geopolymer-like dissolution–precipitation pathway at the interparticle region. The formation of hydrated and carbonated phases has been confirmed by ATR-FTIR and by TGA analysis coupled with the fume FTIR investigation. The total loss of volatile components is about 4 wt%, highlighting that in CSP, only a modest portion of the material undergoes the geopolymerization reaction. Note that the sample processed under the lowest pressure (100 MPa), does not show substantial densification, highlighting that the external pressure is a mandatory requirement to achieve some consolidation, thus differentiating CSP from the traditional geopolymerization of the volcanic ashes.

The key advantages of CSP include: (i) a significant reduction in the energy consumption associated with the firing process compared to conventional sintering; this reduces the environmental footprint of ceramic production; (ii) elimination of additional fluxes and plasticizers, enabling the fabrication of ceramics composed entirely of volcanic ash; this enhances the value of an otherwise underutilized waste material, simultaneously reducing disposal costs; (iii) enhanced material properties, as CSP-derived ceramics exhibit thermal conductivity comparable to standard bricks while achieving a flexural strength up to ~70 MPa, surpassing traditional counterparts.

In conclusion, CSP presents a sustainable and scalable approach for repurposing volcanic ash into ceramics with attractive mechanical and thermal properties. This aligns with circular economy principles and offers a practical solution for waste valorization.

CRediT authorship contribution statement

Vincenzo M. Sglavo: Writing – review & editing, Supervision, Resources. **Danilo Di Genova:** Writing – review & editing, Supervision, Conceptualization. **Milad Kermani:** Supervision, Methodology. **Marco Viccaro:** Writing – review & editing, Methodology. **Levent Karacasulu:** Supervision, Methodology, Investigation. **Mattia Biesuz:** Writing – original draft, Visualization, Validation, Supervision, Resources, Formal analysis, Conceptualization. **Paulina Pazerauskaite:** Writing – original draft, Methodology, Investigation, Formal analysis.

Declaration of Competing Interest

The authors declare that they have no known competing financial interests or personal relationships that could have appeared to influence the work reported in this paper. Mattia Biesuz un behalf of all the authors

Acknowledgements

The authors acknowledge the technical contribution and support of Mr. Adane M. Abebe. D.D.G. acknowledges the funding from the European Research Council (ERC) under the European Union's Horizon Europe research and innovation programme (NANOVOLC, ERC Consolidator Grant – No. 101044772).

Appendix A. Supporting information

Supplementary data associated with this article can be found in the online version at doi:10.1016/j.conbuildmat.2026.145697.

Data availability

Data will be made available on request.

References

[1] J. Dsilva, S. Zarmukhambetova, J. Locke, Assessment of building materials in the construction sector: a case study using life cycle assessment approach to achieve the circular economy, Heliyon 9 (2023) e20404, https://doi.org/10.1016/j.heliyon.2023.e20404.
[2] A. Mollaei, B. Byers, C. Christovan, A. Olumo, C. De Wolf, C. Bachmann, C. Haas, A global perspective on building material recovery incorporating the impact of regional factors, J. Clean. Prod. 429 (2023) 139525, https://doi.org/10.1016/j.jclepro.2023.139525.
[3] B. Huang, X. Gao, X. Xu, J. Song, Y. Geng, J. Sarkis, T. Fishman, H. Kua, J. Nakatani, A life cycle thinking framework to mitigate the environmental impact of building materials, One Earth 3 (2020) 564–573, https://doi.org/10.1016/j.oneear.2020.10.010.
[4] ⟨https://www.eea.europa.eu/en/topics/in-depth/buildings-and-construction⟩, (n. d.).
[5] M. Biesuz, S. Grasso, V.M. Sglavo, What's new in ceramics sintering? A short report on the latest trends and future prospects, Curr. Opin. Solid State Mater. Sci. 24 (2020) 100868, https://doi.org/10.1016/j.cossms.2020.100868.

[6] C. Vakifahmetoglu, L. Karacasulu, Cold sintering of ceramics and glasses: a review, Curr. Opin. Solid State Mater. Sci. 24 (2020) 100807, https://doi.org/10.1016/j.cossms.2020.100807.

[7] S. Grasso, M. Biesuz, L. Zoli, G. Taveri, A.I. Duff, D. Ke, A. Jiang, M.J. Reece, A review of cold sintering processes, Adv. Appl. Ceram. 119 (2020) 115–143, https://doi.org/10.1080/17436753.2019.1706825.

[8] J. Guo, R. Floyd, S. Lowum, J.-P. Maria, T. Herisson de Beauvoir, J.-H. Seo, C. A. Randall, Cold sintering: progress, challenges, and future opportunities, Annu. Rev. Mater. Res. 49 (2019) 275–295, https://doi.org/10.1146/annurev-matsci-070218-010041.

[9] A. Ndayishimiye, M.Y. Sengul, S.H. Bang, K. Tsuji, K. Takashima, T. Hérisson de Beauvoir, D. Denux, J.-M. Thibaud, A.C.T. van Duin, C. Elissalde, G. Goglio, C. A. Randall, Comparing hydrothermal sintering and cold sintering process: mechanisms, microstructure, kinetics and chemistry, J. Eur. Ceram. Soc. 40 (2020) 1312–1324, https://doi.org/10.1016/j.jeurceramsoc.2019.11.049.

[10] J. Guo, H. Guo, A.L. Baker, M.T. Lanagan, E.R. Kupp, G.L. Messing, C.A. Randall, Cold sintering: a paradigm shift for processing and integration of ceramics, Angew. Chem. Int. Ed. 55 (2016) 11457–11461, https://doi.org/10.1002/anie.201605443.

[11] M. Biesuz, G. Taveri, A.I. Duff, E. Olevsky, D. Zhu, C. Hu, S. Grasso, A theoretical analysis of cold sintering, Adv. Appl. Ceram. 119 (2020) 75–89, https://doi.org/10.1080/17436753.2019.1692173.

[12] J. Gonzalez-Julian, K. Neuhaus, M. Bernemann, J. Pereira da Silva, A. Laptev, M. Bram, O. Guillon, Unveiling the mechanisms of cold sintering of ZnO at 250 °C by varying applied stress and characterizing grain boundaries by Kelvin Probe Force Microscopy, Acta Mater. 144 (2018) 116–128, https://doi.org/10.1016/j.actamat.2017.10.055.

[13] H. Guo, A. Baker, J. Guo, C.A. Randall, Cold sintering process: a novel technique for low-temperature ceramic processing of ferroelectrics, J. Am. Ceram. Soc. 99 (2016) 3489–3507, https://doi.org/10.1111/jace.14554.

[14] D. Wang, H. Guo, C.S. Morandi, C.A. Randall, S. Trolier-McKinstry, Cold sintering and electrical characterization of lead zirconate titanate piezoelectric ceramics, APL Mater. 6 (2018) 016101, https://doi.org/10.1063/1.5004420.

[15] A. Sharipova, A. Böhme, M. Fritsch, M. Ahlhelm, A concept for functional bioceramics with embedded metallization using cold sintering, Open Ceram. 21 (2025) 100716, https://doi.org/10.1016/j.oceram.2024.100716.

[16] M. Luginina, R. Orru, G. Cao, D. Grossin, F. Brouillet, G. Chevallier, C. Thouron, C. Drouet, First successful stabilization of consolidated amorphous calcium phosphate (ACP) by cold sintering: toward highly-resorbable reactive bioceramics, J. Mater. Chem. B 8 (2020) 629–635, https://doi.org/10.1039/C9TB02121C.

[17] X. Wang, H. Zhang, X. Yu, X. Mo, J. Gao, Y. Hu, J. Min, Q. Ding, Y. Fan, W. Jiang, Effects of water on cold-sintered highly dense dicalcium phosphate anhydrous bioceramic using its hydrate, J. Am. Ceram. Soc. 107 (2024) 4631–4640, https://doi.org/10.1111/jace.19748.

[18] A. Galotta, F. Agostinacchio, A. Motta, S. Dirè, V.M. Sglavo, Mechanochemical synthesis and cold sintering of mussel shell-derived hydroxyapatite nano-powders for bone tissue regeneration, J. Eur. Ceram. Soc. 43 (2023) 639–647, https://doi.org/10.1016/j.jeurceramsoc.2022.09.024.

[19] H.-J. Kim, T.-H. Kim, J.-M. Oh, F. Salles, G. Chevallier, C. Thouron, P. Trens, J. Soulie, S. Cazalbou, C. Drouet, Cold sintering yields first layered double hydroxides (LDH) monolithic materials, Mater. Sci. Eng. B 280 (2022) 115704, https://doi.org/10.1016/j.mseb.2022.115704.

[20] Y. Zhao, S.S. Berbano, L. Gao, K. Wang, J. Guo, K. Tsuji, J. Wang, C.A. Randall, Cold-sintered V2O5-PEDOT:PSS nanocomposites for negative temperature coefficient materials, J. Eur. Ceram. Soc. 39 (2019) 1257–1262, https://doi.org/10.1016/j.jeurceramsoc.2018.10.018.

[21] R. Boston, J. Guo, S. Funahashi, A.L. Baker, I.M. Reaney, C.A. Randall, Reactive intermediate phase cold sintering in strontium titanate, RSC Adv. 8 (2018) 20372–20378, https://doi.org/10.1039/C8RA03072C.

[22] M. Cao, W.Bin Hong, X.D. Yang, Y.Q. Jia, L. Li, S.Y. Wu, H.S. Yang, X.M. Chen, Dense and strong calcite ceramics prepared by room-temperature cold sintering based on high-pressure-enhanced solubility, J. Am. Ceram. Soc. 106 (2023) 1668–1680, https://doi.org/10.1111/jace.18877.

[23] M. Zahabi, A. Said, A. Memari, Cold sintering of calcium carbonate for construction material applications, ACS Omega 6 (2021) 2576–2588, https://doi.org/10.1021/acsomega.0c04617.

[24] K. Yamaguchi, S. Hashimoto, Mechanism of densification of calcium carbonate by cold sintering process, J. Eur. Ceram. Soc. 42 (2022) 6048–6055, https://doi.org/10.1016/j.jeurceramsoc.2022.06.034.

[25] K. Yamaguchi, S. Hashimoto, Cold sintering of calcium carbonate derived from seashells, Open Ceram. 12 (2022) 100302, https://doi.org/10.1016/j.oceram.2022.100302.

[26] S. Marín-Cortés, M. Biesuz, A. Serrano, E. De Bona, E. Enríquez, J.F. Fernández, V. M. Sglavo, Promoting the circularity of ceramic materials through cold sintering of aggregates from construction and demolition waste, Open Ceram. 20 (2024) 100692, https://doi.org/10.1016/j.oceram.2024.100692.

[27] I. Maruyama, N.K. Bui, A. Meawad, R. Kurihara, Y. Mitani, H. Hyodo, M. Kanematsu, T. Noguchi, Cold-sintered carbonated concrete waste fines: a calcium carbonate concrete block, J. Adv. Concr. Technol. 22 (2024) 406–418, https://doi.org/10.3151/jact.22.406.

[28] E. Kamseu, M. Biesuz, A.-T. Akono, J.N.N. Fokoua, E. De Bona, N. Buettner, H. Lee, C. Leonelli, S. Rossignol, V.M. Sglavo, Cold-sintered laterite-based geopolymers: densification, microstructure and micromechanics, J. Eur. Ceram. Soc. 44 (2024) 116798, https://doi.org/10.1016/j.jeurceramsoc.2024.116798.

[29] L. Lattanzi, A. Conte, A. Sin, J.M. Garcia, C.A. Randall, P. Colombo, Cold sintering of geopolymer powders, J. Am. Ceram. Soc. (2024), https://doi.org/10.1111/jace.20331.

[30] K. Nishikawa, S. Hashimoto, H. Imai, S. Rossignol, Cold reaction sintering for preparation of ultra-dense geopolymer products, Constr. Build. Mater. 328 (2022) 127101, https://doi.org/10.1016/j.conbuildmat.2022.127101.

[31] O.A. Radwan, M.A. Hussein, R.A. Assaggaf, J.D. Humphrey, M. Al-Hashem, A. A. Mahmoud, Rebuilding with sand roses: cold sintering of sand-gypsum mixture for sustainable brick production, Constr. Build. Mater. 442 (2024) 137642, https://doi.org/10.1016/j.conbuildmat.2024.137642.

[32] R.V. Fisher, H.-U. Schmincke, Pyroclastic Rocks, Springer-Verlag, Berlin Heidelberg New York Tokyo, 1984, https://doi.org/10.1007/978-3-642-74864-6.

[33] G. Heiken, K. Wohletz, Volcanic ash, Cambridge University Press, 1986 https://doi.org/DOI: 10.1017/S0016756800033719.

[34] M. Polacci, D. Andronico, M. de' Michieli Vitturi, J. Taddeucci, A. Cristaldi, Mechanisms of ash generation at basaltic volcanoes: the case of Mount Etna, Italy, Front. Earth Sci. 7 (2019), https://doi.org/10.3389/feart.2019.00193.

[35] D. Di Genova, R.A. Brooker, H.M. Mader, J.W.E. Drewitt, A. Longo, J. Deubener, D. R. Neuville, S. Fanara, O. Shebanova, S. Anzellini, F. Arzilli, E.C. Bamber, L. Hennet, G. La Spina, N. Miyajima, In situ observation of nanolite growth in volcanic melt: a driving force for explosive eruptions, Sci. Adv. 6 (2020), https://doi.org/10.1126/sciadv.abb0413.

[36] T.M. Wilson, C. Stewart, V. Sword-Daniels, G.S. Leonard, D.M. Johnston, J.W. Cole, J. Wardman, G. Wilson, S.T. Barnard, Volcanic ash impacts on critical infrastructure, Phys. Chem. Earth 4546 (2012) 5–23, https://doi.org/10.1016/j.pce.2011.06.006.

[37] S.F. Jenkins, T.M. Wilson, C. Magill, V. Miller, C. Stewart, R. Blong, W. Marzocchi, M. Boulton, C. Bonadonna, A. Costa, Volcanic ash fall hazard and risk, in: S. C. Loughlin, S. Sparks, S.K. Brown, S.F. Jenkins, C. Vye-Brown (Eds.), Global Volcanic Hazards and Risk, Cambridge University Press, Cambridge, 2015, pp. 173–222, https://doi.org/DOI: 10.1017/CBO9781316276273.005.

[38] T.M. Wilson, J.W. Cole, C. Stewart, S.J. Cronin, D.M. Johnston, Ash storms: impacts of wind-remobilised volcanic ash on rural communities and agriculture following the 1991 Hudson eruption, southern Patagonia, Chile, Bull. Volcano 73 (2011) 223–239, https://doi.org/10.1007/s00445-010-0396-1.

[39] G. Gudmundsson, Respiratory health effects of volcanic ash with special reference to Iceland. A review, Clin. Respir. J. 5 (2011) 2–9, https://doi.org/10.1111/j.1752-699X.2010.00231.x.

[40] F. Prata, B. Rose, Chapter 52 - Volcanic Ash Hazards to Aviation, in: H. Sigurdsson (Ed.), The Encyclopedia of Volcanoes (Second Edition), Second Edition, Academic Press, Amsterdam, 2015, pp. 911–934, https://doi.org/10.1016/B978-0-12-385938-9.00052-3.

[41] M. Mazzocchi, F. Hansstein, M. Ragona, The 2010 volcanic ash cloud and its financial impact on the European Airline Industry, CESifo Forum 11 (2010) 92–100.

[42] T.J. Casadevall, The 1989–1990 eruption of Redoubt Volcano, Alaska: impacts on aircraft operations, J. Volcanol. Geotherm. Res. 62 (1994) 301–316, https://doi.org/10.1016/0377-0273(94)90038-8.

[43] M. Giuffrida, M. Cardone, F. Zuccarello, M. Viccaro, Etna 2011–2022: discoveries from a decade of activity at the volcano, Earth. Sci. Rev. 245 (2023) 104563, https://doi.org/10.1016/j.earscirev.2023.104563.

[44] M. Giuffrida, M. Viccaro, Three years (2011–2013) of eruptive activity at Mt. Etna: working modes and timescales of the modern volcano plumbing system from micro-analytical studies of crystals, Earth. Sci. Rev. 171 (2017) 289–322, https://doi.org/10.1016/j.earscirev.2017.06.003.

[45] D. Andronico, A. Cannata, G. Di Grazia, F. Ferrari, The 1986–2021 paroxysmal episodes at the summit craters of Mt. Etna: insights into volcano dynamics and hazard, Earth. Sci. Rev. 220 (2021) 103686, https://doi.org/10.1016/j.earscirev.2021.103686.

[46] S. Scollo, M. Coltelli, C. Bonadonna, P. Del Carlo, Tephra hazard assessment at Mt. Etna (Italy), Nat. Hazards Earth Syst. Sci. 13 (2013) 3221–3233, https://doi.org/10.5194/nhess-13-3221-2013.

[47] C.M. Belfiore, C. Amato, A. Pezzino, M. Viccaro, An end of waste alternative for volcanic ash: a resource in the manufacture of ceramic tiles, Constr. Build. Mater. 263 (2020) 120118, https://doi.org/10.1016/j.conbuildmat.2020.120118.

[48] M. Cavalieri, P.L. Ferrara, C. Finocchiaro, M.F. Martorana, An Economic Analysis of the Use of Local Natural Waste: volcanic Ash of Mt. Etna Volcano (Italy) for Geopolymer Production, Sustainability 16 (2024) 740, https://doi.org/10.3390/su16020740.

[49] L. Contrafatto, Volcanic ash. Sustainable Concrete Made with Ashes and Dust from Different Sources, Elsevier, 2022, pp. 331–418, https://doi.org/10.1016/B978-0-12-824050-2.00011-5.

[50] G. Cultrone, The use of Mount Etna volcanic ash in the production of bricks with good physical-mechanical performance: converting a problematic waste product into a resource for the construction industry, Ceram. Int. 48 (2022) 5724–5736, https://doi.org/10.1016/j.ceramint.2021.11.119.

[51] S.S. Eldera, S. Aldawsari, E.M.A. Hamzawy, Utilization of waste glass with natural pozzolan in the production of self-glazed glass-ceramic materials, Nanotechnol. Rev. 12 (2023), https://doi.org/10.1515/ntrev-2022-0565.

[52] A. Játiva, E. Ruales, M. Etxeberria, Volcanic ash as a sustainable binder material: an extensive review, Materials 14 (2021) 1302, https://doi.org/10.3390/ma14051302.

[53] A. Karamanov, S. Ergul, M. Akyildiz, M. Pelino, Sinter-crystallization of a glass obtained from basaltic tuffs, J. Non Cryst. Solids 354 (2008) 290–295, https://doi.org/10.1016/j.jnoncrysol.2007.07.040.

[54] P.N. Lemougna, K. Wang, Q. Tang, A.N. Nzeukou, N. Billong, U.C. Melo, X. Cui, Review on the use of volcanic ashes for engineering applications, Resour. Conserv. Recycl 137 (2018) 177–190, https://doi.org/10.1016/j.resconrec.2018.05.031.

[55] S.E. Zafarana, P. Scanferla, C. Finocchiaro, G. Barone, P. Mazzoleni, J. Kraxner, D. Galusek, Influence of activator molarity and waste-glass-to-volcanic-ash ratios on the microstructure of potassium-based alkali-activated pastes, J. Solgel Sci. Technol. 116 (2025) 1614–1629, https://doi.org/10.1007/s10971-025-06937-9.
[56] G. Barone, C. Finocchiaro, I. Lancellotti, C. Leonelli, P. Mazzoleni, C. Sgarlata, A. Stroscio, Potentiality of the use of pyroclastic volcanic residues in the production of alkali activated material, Waste Biomass.. Valoriz. 12 (2021) 1075–1094, https://doi.org/10.1007/s12649-020-01004-6.
[57] C. Finocchiaro, G. Barone, P. Mazzoleni, C. Leonelli, A. Gharzouni, S. Rossignol, FT-IR study of early stages of alkali activated materials based on pyroclastic deposits (Mt. Etna, Sicily, Italy) using two different alkaline solutions, Constr. Build. Mater. 262 (2020) 120095, https://doi.org/10.1016/j.conbuildmat.2020.120095.
[58] P. Scanferla, C. Finocchiaro, A. Gharzouni, G. Barone, P. Mazzoleni, S. Rossignol, High temperature behavior of sodium and potassium volcanic ashes-based alkali-activated materials (Mt. Etna, Italy), Constr. Build. Mater. 408 (2023) 133702, https://doi.org/10.1016/j.conbuildmat.2023.133702.
[59] C. Finocchiaro, G. Barone, P. Mazzoleni, G. Cultrone, Insight on physical–mechanical properties of one-part alkali-activated materials based on volcanic deposits of Mt. Etna (Italy) and their durability against ageing tests, Mater. Struct. 57 (2024) 198, https://doi.org/10.1617/s11527-024-02471-2.
[60] L. Contrafatto, Recycled Etna volcanic ash for cement, mortar and concrete manufacturing, Constr. Build. Mater. 151 (2017) 704–713, https://doi.org/10.1016/j.conbuildmat.2017.06.125.
[61] C.M. Belfiore, S. Parisi, S. Menta, P. Mazzoleni, Use of volcanic ash and chamotte as substitute temper in the production of ceramic tiles, Appl. Clay Sci. 262 (2024) 107603, https://doi.org/10.1016/j.clay.2024.107603.
[62] M. Fugazzotto, R. Occhipinti, M.C. Caggiani, A. Coccato, C. Finocchiaro, G. Lanzafame, P. Mazzoleni, G. Nucatolo, G. Piacenti, S. Starinieri, A. Stroscio, G. Barone, Restoration feasibility study by using alkali activated mortars based on Mt. Etna volcanic ash: the case study of Monreale Cathedral (Palermo, Italy), Mater. Lett. 333 (2023) 133626, https://doi.org/10.1016/j.matlet.2022.133626.
[63] T. Ibn-Mohammed, C.A. Randall, K.B. Mustapha, J. Guo, J. Walker, S. Berbano, S.C. L. Koh, D. Wang, D.C. Sinclair, I.M. Reaney, Decarbonising ceramic manufacturing: a techno-economic analysis of energy efficient sintering technologies in the functional materials sector, J. Eur. Ceram. Soc. 39 (2019) 5213–5235, https://doi.org/10.1016/j.jeurceramsoc.2019.08.011.
[64] D. Sohrabi Baba Heidary, M. Lanagan, C.A. Randall, Contrasting energy efficiency in various ceramic sintering processes, J. Eur. Ceram. Soc. 38 (2018) 1018–1029, https://doi.org/10.1016/j.jeurceramsoc.2017.10.015.
[65] S.H. Bang, K. Tsuji, A. Ndayishimiye, S. Dursun, J.-H. Seo, S. Otieno, C.A. Randall, Toward a size scale-up cold sintering process at reduced uniaxial pressure, J. Am. Ceram. Soc. 103 (2020) 2322–2327, https://doi.org/10.1111/jace.16976.
[66] A. Jabr, H.N. Jones, A.P. Argüelles, S. Trolier-McKinstry, C. Randall, R. Bermejo, Scaling up the cold sintering process of ceramics, J. Eur. Ceram. Soc. 43 (2023) 5319–5329, https://doi.org/10.1016/j.jeurceramsoc.2023.04.061.
[67] J.G.C. Ball, B.E. Reed, R.G. Grainger, D.M. Peters, T.A. Mather, D.M. Pyle, Measurements of the complex refractive index of volcanic ash at 450, 546.7, and 650 nm, J. Geophys. Res. Atmos. 120 (2015) 7747–7757, https://doi.org/10.1002/2015JD023521.
[68] D.K. Shetty, A.R. Rosenfield, P. McGuire, G.K. Bansal, W.H. Duckworth, Biaxial flexure tests for ceramics, Am. Ceram. Soc. Bull.;(United States) 59 (1980).
[69] L. Karacasulu, D. Karl, A. Gurlo, C. Vakifahmetoglu, Cold sintering as a promising ISRU technique: a case study of Mars regolith simulant, Icarus 389 (2023) 115270.
[70] J. Serra, P. González, S. Liste, C. Serra, S. Chiussi, B. León, M. Pérez-Amor, H. O. Ylänen, M. Hupa, FTIR and XPS studies of bioactive silica based glasses, J. Non Cryst. Solids 332 (2003) 20–27, https://doi.org/10.1016/j.jnoncrysol.2003.09.013.
[71] M. Cassetta, G.D. Sorarù, E. Callone, S. Dirè, A.M. Abebe, S. Mariazzi, R.S. Brusa, M. Giarola, N. Daldosso, M. Biesuz, From SiO1.5CH3 to vitreous SiO2: a structural evolution study, J. Non Cryst. Solids 648 (2025) 123327, https://doi.org/10.1016/j.jnoncrysol.2024.123327.
[72] T.L. Hughes, C.M. Methven, T.G.J. Jones, S.E. Pelham, P. Fletcher, C. Hall, Determining cement composition by Fourier transform infrared spectroscopy, Adv. Cem. Based Mater. 2 (1995) 91–104, https://doi.org/10.1016/1065-7355(94)00031-X.
[73] S. Scollo, M. Coltelli, C. Bonadonna, P. Del Carlo, Tephra hazard assessment at Mt. Etna (Italy), Nat. Hazards Earth Syst. Sci. 13 (2013) 3221–3233, https://doi.org/10.5194/nhess-13-3221-2013.
[74] B. Santhosh, A. Galotta, G.D. Sorarù, V.M. Sglavo, M. Biesuz, Cold sintering of colloidal silica particles using different alkali solutions, Ceram. Int. 48 (2022) 35627–35632, https://doi.org/10.1016/j.ceramint.2022.08.334.
[75] S. Kang, X. Zhao, J. Guo, Y. Xiao, Y. Yang, B. He, X. Wang, L. Yang, R. Liao, Evolution from transparent SiO2 glass to ceramics enabled by cold sintering with a transient chemistry: H2SiO3, Scr. Mater. 233 (2023) 115522, https://doi.org/10.1016/j.scriptamat.2023.115522.
[76] A. Galotta, E. Giust, M. Bortolotti, G.D. Sorarù, V.M. Sglavo, M. Biesuz, Cold sintering of diatomaceous earth, J. Am. Ceram. Soc. 104 (2021) 4329–4340, https://doi.org/10.1111/jace.17863.
[77] R.H. Doremus, Glass Science, II, 1994.
[78] R.A. Maier, In situ observation of the multistep process of cold sintering, J. Am. Ceram. Soc. 107 (2024) 6544–6553, https://doi.org/10.1111/jace.19947.
[79] A. Jabr, J. Fanghanel, Z. Fan, R. Bermejo, C. Randall, The effect of liquid phase chemistry on the densification and strength of cold sintered ZnO, J. Eur. Ceram. Soc. 43 (2023) 1531–1541, https://doi.org/10.1016/j.jeurceramsoc.2022.11.071.
[80] A. Jabr, S.D. Škapin, S. Tominc, N. Daneu, J. König, V. Ducman, L.K. Bensa, R. Bermejo, M. Spreitzer, Enhancing densification of metakaolin-based geopolymers via the cold sintering process, Open Ceram. 24 (2025) 100863, https://doi.org/10.1016/j.oceram.2025.100863.
[81] W.D. Kingery, H.K. Bowen, D.R. Uhlmann, Introduction to Ceramics, Second, Wiley, New York (USA), 1976, https://doi.org/10.1037/023990.
[82] S. Ni, H. Liu, Q. Li, H. Quan, M. Gheibi, A.M. Fathollahi-Fard, G. Tian, Assessment of the engineering properties, carbon dioxide emission and economic of biomass recycled aggregate concrete: a novel approach for building green concretes, J. Clean. Prod. 365 (2022) 132780, https://doi.org/10.1016/j.jclepro.2022.132780.
[83] M. Kubiś, K. Pietrak, Ł. Cieślikiewicz, P. Furmański, M. Wasik, M. Seredyński, T. S. Wiśniewski, P. Łapka, On the anisotropy of thermal conductivity in ceramic bricks, J. Build. Eng. 31 (2020) 101418, https://doi.org/10.1016/j.jobe.2020.101418.
[84] J. García Ten, M.J. Orts, A. Saburit, G. Silva, Thermal conductivity of traditional ceramics. Part I: influence of bulk density and firing temperature, Ceram. Int. 36 (2010) 1951–1959, https://doi.org/10.1016/j.ceramint.2010.05.012.
[85] S. Karaman, E. Sabit, G. Hikmet, Firing temperature and firing time influence on mechanical and physical properties of clay bricks, J. Sci. Ind. Res. (India). 65 (2006) 153–159.
[86] J. Cai, N. Lv, X. Jia, R. Zhang, G. Xu, L. Cai, Q. Tian, Properties of permeable ceramic brick prepared with felsite tailing, J. Build. Eng. 44 (2021) 103426, https://doi.org/10.1016/j.jobe.2021.103426.
[87] C.L. Cramer, E. Lara-Curzio, A.M. Elliott, T.G. Aguirre, B. Yoon, B.A. Fricke, V. Rao, P. Jain, K. Nawaz, Material selection and manufacturing for high-temperature heat exchangers: review of state-of-the-art development, opportunities, and challenges, Int. J. Ceram. Eng. Sci. 6 (2024), https://doi.org/10.1002/ces2.10230.
[88] L. Karacasulu, E. Ogur, C. Piskin, C. Vakifahmetoglu, Cold sintering of soda-lime glass, Scr. Mater. 192 (2021) 111–114, https://doi.org/10.1016/j.scriptamat.2020.10.015.
[89] J.D. Hunt, A. Kavner, E.A. Schauble, D. Snyder, C.E. Manning, Polymerization of aqueous silica in H2O–K2O solutions at 25–200°C and 1bar to 20kbar, Chem. Geol. 283 (2011) 161–170, https://doi.org/10.1016/j.chemgeo.2010.12.022.
[90] A. Galotta, V.M. Sglavo, The cold sintering process: a review on processing features, densification mechanisms and perspectives, J. Eur. Ceram. Soc. 41 (2021) 1–17, https://doi.org/10.1016/j.jeurceramsoc.2021.09.024.
[91] J.N.Y. Djobo, A. Elimbi, H.K. Tchakouté, S. Kumar, Reactivity of volcanic ash in alkaline medium, microstructural and strength characteristics of resulting geopolymers under different synthesis conditions, J. Mater. Sci. 51 (2016) 10301–10317, https://doi.org/10.1007/s10853-016-0257-1.
[92] P. Duxson, S.W. Mallicoat, G.C. Lukey, W.M. Kriven, J.S.J. van Deventer, The effect of alkali and Si/Al ratio on the development of mechanical properties of metakaolin-based geopolymers, Colloids Surf. A Physicochem. Eng. Asp. 292 (2007) 8–20, https://doi.org/10.1016/j.colsurfa.2006.05.044.
[93] M. Kamath, S. Prashant, R. Ralegaonkar, Microstructure properties of popular alkali-activated pastes cured in ambient temperature, Buildings 13 (2023) 858.
[94] I. Garcia-Lodeiro, A. Palomo, A. Fernández-Jiménez, D.E. Macphee, Compatibility studies between N-A-S-H and C-A-S-H gels. Study in the ternary diagram Na2O–CaO–Al2O3–SiO2–H2O, Cem. Concr. Res. 41 (2011) 923–931, https://doi.org/10.1016/j.cemconres.2011.05.006.